Suppressing the Thrust Ripple of the Consequent-Pole Permanent Magnet Linear Synchronous Motor by Two-Step Design

XUZHEN HUANG[1], **(Member, IEEE), JING LIANG**[1], **BO ZHOU**[1], **CHENGMING ZHANG**[2], **LIYI LI**[2], **(Member, IEEE), AND DAVID GERADA**[3]

[1]Department of Electrical Engineering, Nanjing University of Aeronautics and Astronautics, Nanjing 211111, China
[2]Department of Electrical Engineering, Harbin Institute of Technology, Harbin 150001, China
[3]Department of Electrical Engineering, University of Nottingham, Nottingham GN7 2RD, U.K.

Corresponding author: Xuzhen Huang (huangxuzhen@nuaa.edu.cn)

ABSTRACT This paper investigates the thrust ripple of a consequent-pole permanent magnet linear synchronous motor (CP-PMLSM). The components of the thrust ripple are analyzed through the comparison of the thrust waves' constituent frequencies. A two-step design process is then proposed in order to reduce the different components of the thrust ripple. The first step consists of implementing a modular regulating structure and rewinding the coils in the resulting two sectional motors, through which the thrust ripples of the modular CP-PMLSM originating from the armature current and voltage harmonics are suppressed. In the second step, the geometrical parameters defining the magnetic regulating structure and the end-teeth are comprehensively optimized to reduce the detent force. By using the aforesaid procedure, it is shown that the CP-PMLSM can achieve small values of thrust ripple for different loadings.

INDEX TERMS Detent force, linear motor, modular, optimization, permanent magnet motor, thrust ripple.

I. INTRODUCTION

High performance linear-motion applications often require loads that can be driven directly thus eliminating the need for intermediate conversion mechanisms. For the direct-drive permanent magnet linear synchronous motor (PMLSM) system, motion range is determined by the length of the primary and secondary. Furthermore it is difficult to improve the power density by using a large gear-reduction ratio. Consequently, for applications requiring a long distance and a high thrust, the volume and mass of the PMLSM are typically substantially big resulting in a costlier scheme with respect to that of combining rotary motors with reduction mechanisms. For a PMLSM with a long secondary, the cost of the permanent magnets may well be in excess of 50% of all the material cost.

Single-sided flat linear motors have a couple of problematic features due to the iron-core in the mover. One of them is the normal force which typically ranges from 5 to 10 times of the rated thrust, thus a set of linear bearings with a high stiffness are normally required. The other problematic feature is the detent force, which is a periodic fluctuant force rooted in two sources: the first source is the effect between stator slots and poles, while the second source is the end-effect which produces a pulsating force component acting on the teeth at both ends of the mover. The latter is often considered to be the most dominant ripple component in PMSLMs [1].

This paper applies the consequent pole (CP) topology to the single-sided PMLSM. So far, the novel consequent pole topology has received wide attention and has been applied in several types of machines, such as vernier machines [2]–[4], flux-switching machines [5], reverse flux machines [6], magnetic levitation machines [7]–[8], and permanent magnet synchronous machines (PMSM) [9]–[11]. Compared to the typical North-South (NS) pole, each pair of poles consists of one PM pole and one core pole. In this case, a magnetic pole with opposite magnetism with respect to the PM appears in the core pole. It was analytically explored that the PMLSMs with a consequent pole stator and a specially designed mover structure can effectively reduce the magnetic unbalance and end effects while retaining good thrust linearity, and reducing the amount of PM material [12]. Moreover, the core pole contributes to the strengthening of
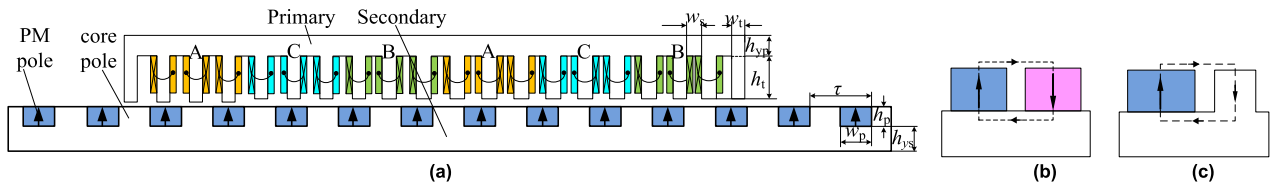
FIGURE 1. Structure of PMLSM and poles; (a) CP-PMLSM. (b) NS-pole. (c) Consequent pole.

the secondary thus helping in reducing the mover back-iron thickness and the mass of the secondary.

The aforementioned problem of detent force can also limit the use of the CP-PMLSM particularly when it comes to high precision applications. Furthermore the CP-PMLSM has a doubly salient construction which tends to enlarge the thrust ripple. Consequently, reducing the thrust ripple is one of the key aspects for the successful application uptake of the CP-PMLSM.

Theoretically, typical thrust ripple suppression methods that have been adopted by the PMLSM with a traditional pole structure can also be applied to the consequent-pole PMLSM. These methods can be divided into three main categories. The first category involves optimizing the pole or slot distribution as in [13]–[15]. For example, in [13] unequal pole-arc coefficients were set in a long-stator PMLSM to reduce the cogging force. Trapezoidal and convex poles were also researched to improve the magnetic field distribution in [14], while in [15] a magnet-shifting method was applied to a double-side PMSLM. The second category involves optimizing the end structure or core length to suppress the end effects [16]–[18]. In [16] it was shown that the end effect could be reduced without excessive stator length extension if a slot-less stator with two different lengths is employed, while in [17], a modular primary iron-core PMSLM with an increased number of core ends was investigated and used to achieve a low thrust ripple. The third category of adopted approaches involves setting a compensation winding or applying compensation control to reduce the thrust and velocity ripple [18], [19].

The consequent pole topology under investigation in this research gives rise to some further special harmonics which lead to a marked rise of thrust ripple and ripple-ratio with the increase of load. In this paper, the scheme of a modular CP- PMLSM is proposed to overcome the aforesaid issue. Section II analyzes the structure and thrust characteristics of the traditional CP-PMLSM. A two-step design is proposed based on two dimensional (2-D) finite-element (FEM) analysis in Section III and IV. The modular structure is presented in Section III, followed by the optimization of the magnetic regulating structure in Section IV. Section V reports on the developed CP-PMLSM prototype and test results. Finally, conclusions are drawn in Section VI.

II. THRUST CHARACTERISTIC OF DIFFERENT PMLSMS
A. THEORY OF THE THRUST RIPPLE
Fig. 1 shows the structures of a 20-pole 18-slot PMLSM and the different pole structures. The motor includes both the

TABLE 1. Parameters of the CP-PMLSM.

Symbol	ITEMS	CP-PMLSM	NS-PMLSM
P	Number of poles	20	20
Q	Number of slots	18	18
τ	Pole pitch (mm)	8.1	8.1
w_p	Width of PM (mm)	8.6	6.5
h_p	Height of PM (mm)	2.5	2.5
h_t	Height of teeth (mm)	11.4	11.4
w_t	Width of teeth (mm)	4.4	4.4
w_s	Width of slot (mm)	4.6	4.6
h_yp	Height of primary yoke (mm)	3	3
h_ys	Height of secondary yoke (mm)	9	14.5
N	Number of coils per phase	138	138
L	Laminated length (mm)	100	100

primary and secondary. For the PMLSM with CP structure, one PM pole in the secondary is set between two core poles which results in a doubly salient structure. Contrary to the traditional NS pole structure, the magnetic directions of all the PMs are the same. When the secondary employs the CP structure, the linear motor is a CP-PMLSM. Similarly, if the NS-Poles are used, it is a NS-PMLSM. The primaries of them are the same, consisting of a fractional-slot double-layer concentrated winding. The parameters of the CP-PMLSM and NS-PMLSM are listed in Table 1. The FEM model is established, and the flux distribution of the CP-PMLSM on no-load condition is shown in Fig. 2. The flux generated by the PMs crosses the airgap, the primary core, the core pole, and secondary yoke, thus forming closed loops.
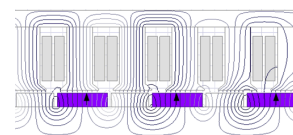

FIGURE 2. Flux distribution of the CP-PMLSM.

As mentioned before, the end effect, slot effect and voltage of current harmonics cause the thrust ripple together. For the short primary linear motor which employs the surface permanent magnet and fractional slot structures, the cogging force which dues to the slot effect is much lower than the detent force. Previous research analytically investigated and discussed the end-effect detent force, which is the dominant component of the thrust ripple for the NS-PMLSM. The

physical representation was provided as follows [20]–[22]:

$$f_{\text{detent}} = f_+ + f_- = \sum_{n=1}^{\infty} F_n \sin \frac{2n\pi}{\tau}(z + \frac{\tau}{2}) \qquad (1)$$

$$F_n = 2\left(F_{sn} \cos \frac{n\pi}{\tau}\Delta + F_{cn} \sin \frac{n\pi}{\tau}\Delta\right), \quad (\Delta = L_s - n\tau) \qquad (2)$$

where f_+ and f_- denote the force at the right and left end, F_{sn} and F_{cn} denote the amplitudes of the n-th sinusoidal and cosinoidal components respectively. L_s is the length of the primary core, τ is the pole pitch.

Suppose that the resistance of the windings can be ignored, the single-phase current and voltage can be expressed as (3) and (4) respectively.

$$i_K(t) = I_{m1} \sin(\omega t + \alpha_K) \qquad (3)$$

$$e_K(t) = \sum_{i=1}^{\infty} E_{mi} \sin(i\omega t + \beta_{Ki}) \qquad (4)$$

where $i_K(t)$ and $e_K(t)$ are the current and voltage of phase K (for a three-phase motor, K can represents phases A, B and C). I_{m1} and α_K indicate the amplitude and electrical angle of the fundamental current. E_{mi} and β_{Ki} indicate the amplitude and electrical angle of i-th voltage harmonic.

The output force f of each phase that includes the direct component (also referred-to as the average thrust) and ripple thrust can be calculated by

$$f = i_K(t) \cdot e_K(t)/v \qquad (5)$$

where v denotes the mover velocity.

Therefore the current and voltage components which are with different frequencies act together and generate the thrust ripple.

B. SIMULATION OF THE THRUST CHARACTERISTICS

Fig. 3 shows the thrust characteristics. When the current along q-axis is exerted, the thrust will reach the maximum. With the parameters as listed in Table 1, the average thrust of consequent-pole PMLSM is about 83% of that of the typical NS-pole PMLSM. At the moment the permanent magnet dosage of the CP-PMLSM is about 66.2% of that of the NS-PMLSM. For the CP-PMLSM, if the height of the PM is increased to 3.5 mm, the average thrust is close to that of the NS-PMLSM. But the permanent magnet mass will increase to about 92.6% of the NS-PMLSM's.

In general, the CP-PMLSM can save permanent magnet. Different from the NS-PMLSM, the thrust ripple of the CP-PMLSM increases as the current. The thrust ripple of the CP-PMLSM is slightly smaller than that of the NS-pole motor in case of no load and low load condition, but it increases significantly with the increase of load current.

The period of the end-effect detent force can be considered as 180°. Fig. 3 (a) shows the thrust curves of the PMLSMs with consequent pole and NS pole when operated at the rated load (the current density is 6.9 A/mm^2). For the
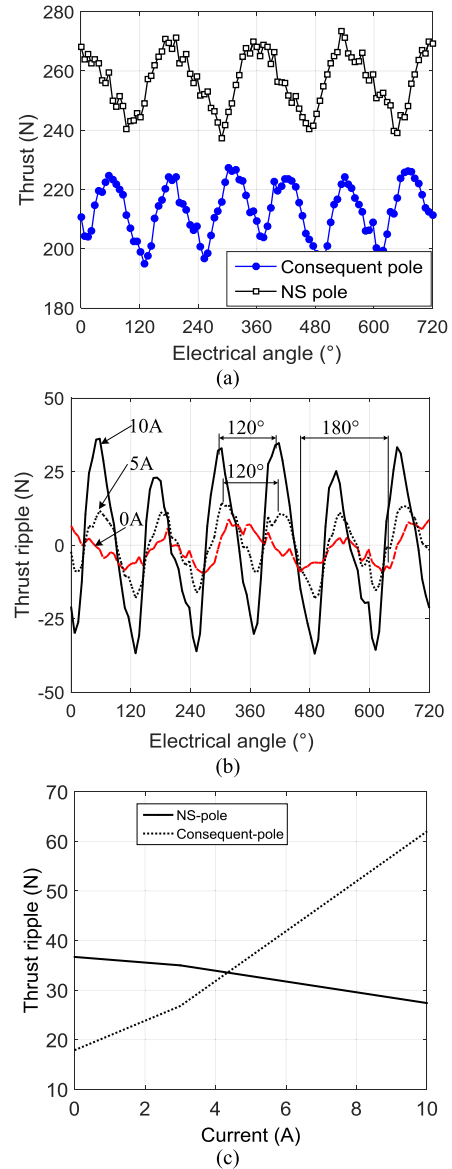

FIGURE 3. Thrust characteristics. (a) Thrust waveforms in rated condition. (b) Thrust ripple curves of the CP-PMLSM; (c) Peak-to-peak values of thrust ripple.

NS-pole PMLSM which is with the same structure parameters except the pole, the electrical angle between two fluctuations is about 180°. However, when the primary of the CP-PMLSM moves along the electrical angle 0° to 720° (the primary is used for the mover), the frequency of the thrust fluctuation is 6 times, hence the electrical angle between two peaks is about 120°, which is different from that of the NS-pole PMLSM. To further analyze this difference, the thrust ripple curves when the windings carry different currents are shown in period of 180°, which concurs with (1). However, the fluctuating frequencies of the thrust ripple change as the armature currents are applied. The thrust waves follow a 120° cycle when the current is 5 A or 10 A.

Also importantly, the amplitude of the thrust ripple increases almost linearly with the current. This phenomenon

is related to the armature reaction, or more specifically to the current and voltage harmonics. In the FEM model established, the current waveform is an ideal sinusoid, hence the voltages including all the constituent harmonics act together with the fundamental current. The amplitudes of the voltage harmonics are shown in Fig. 4. Fundamental component apart, the maximal harmonic component of the voltage is the second harmonic. Hence the combined action of the fundamental current with the second voltage harmonic produces the third-order thrust ripple, the fluctuating period of which is about 120°. That is why the thrust ripple of the CP-PMLSM increase as the current.
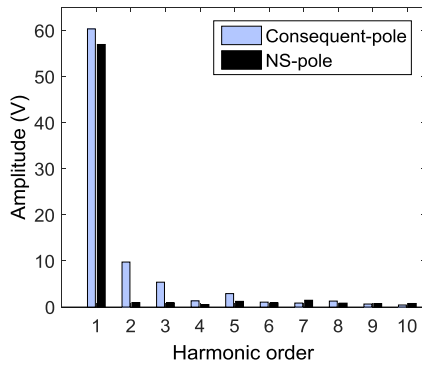

FIGURE 4. Harmonic components of voltage waveform.

III. MODULAR AND WINDING SHIFTING DESIGN TO ADJUST THRUST RIPPLE–STEP I

To inhibit the thrust ripple that is caused by the voltage harmonics, a modular CP-PMLSM with a shifting winding structure is proposed in this paper. As shown in Fig. 5, a magnetic regulating structure the width of which is $k\tau$ (where k is an odd number and usually selected as 1 to limit the volume of the primary) is introduced between the primary cores of two sectional motors (Motor I and Motor II are corresponding to section I and section II, respectively). Furthermore the coils belonging to the same phase in these two motors are wound in reverse order, as shown by the coil go (●) and return (X) marks in Fig. 5.

The winding voltage of each sectional motor can be expressed as the superposition of odd and even order harmonics. For Motor I the voltage can be calculated by

$$u_{i1} = \sum_{n}^{n=1,3,5\cdots} U_{nm}\sin(n\omega t + \theta_n) + \sum_{j}^{j=2,4,6\cdots} U_{jm}\sin(j\omega t + \theta_j) \quad (6)$$

where U_{nm} and U_{jm} are the amplitudes of the n-th and j-th harmonics, θ_n and θ_j are the initial electrical degrees.

On the other hand for Motor II, if the influence of the end effect is ignored, the voltage of the same phase winding u_{i2}

can be represented as follows:

$$u_{i2} = \sum_{n}^{n=1,3,5\cdots} U_{nm}\sin(n(\omega t + \pi) + \theta_n + \pi)$$
$$+ \sum_{j}^{j=2,4,6\cdots} U_{jm}\sin(j(\omega t + \pi) + \theta_j + \pi) \quad (7)$$

Comparing equations (6) and (7), it can be concluded that the phase difference of odd-order harmonics belonging to the same phase in the different sectional motors is $\Phi_1 = (n+1)\pi$. In this case, Φ_1 is the sum of $n\pi$ and π where the former is the result of the reversal of the winding, whereas the latter is the phase regulating function of the introduced magnetic regulating structure. Since n and 1 are both odd numbers, the addition of n and 1 always results in an even number.

Similarly, the phase difference of even-order harmonics belonging to the same phase in the different sectional motors is $\Phi_2 = (j + 1)\pi$. Since j is an even number and 1 is an odd number, the addition of j and 1 always results in an odd number. The resultant voltage of the same phase windings from the two sectional motors is the sum of u_{i1} and u_{i2}:

$$u_i = u_{i1} + u_{i2}$$
$$= \sum_{n}^{n=1,3,5\cdots} U_{nm}[\sin(n\omega t + \theta_n) + \sin(n\omega t + \theta_n + \phi_1)]$$
$$+ \sum_{j}^{j=2,4,6\cdots} U_{jm}[\sin(j\omega t + \theta_j) + \sin(j\omega t + \theta_j + \phi_2)] \quad (8)$$

$$\begin{cases} \phi_1 = (n+1)\pi = 2M \cdot \pi \\ \phi_2 = (j+1)\pi = (2N+1) \cdot \pi \end{cases} \quad (9)$$

where M and N are natural numbers.

Thus it can be observed that by designing the magnetic regulating structure and reversing the windings, the even-order harmonics of Motor I are offset by those of Motor II, hence the even harmonic contents become smaller in magnitude. On the other hand, the fundamental and odd-order harmonic contents remain unchanged, so the average thrust will not be reduced.

If non-magnetic material is adopted for the magnetic regulating structure, the no-load back EMF and on-load voltage waveforms of the sectional motors can be calculated, together with their additions as shown in Fig. 6. In the aforesaid figure, AI and AII refer to the windings of phase A in sectional motors I and II respectively. Comparing Figs. 6(a) and 6(b), it is evident that the armature current gives rise to an increasing amount of the high-order voltage harmonics on each sectional motor.

Fig. 7 analyzes the harmonics of the on-load voltage waveforms. For phase A of the whole modular motor (i.e. AI+AII), the fundamental remains essentially constant upon adding the contributions of the two sectional motors. However, the 2nd harmonic is markedly reduced, which has a significant influence on the thrust wave, as shown in Fig. 8. In fact, the average thrust of the modular CP- PMLSM is a little
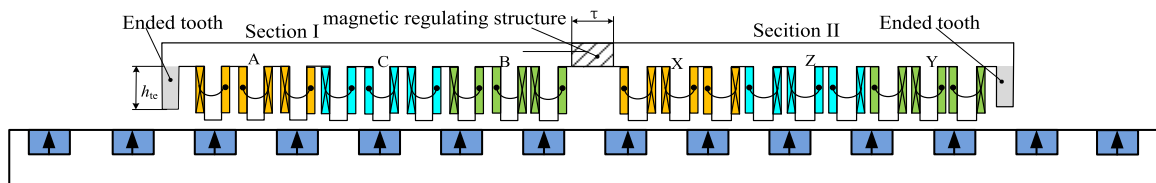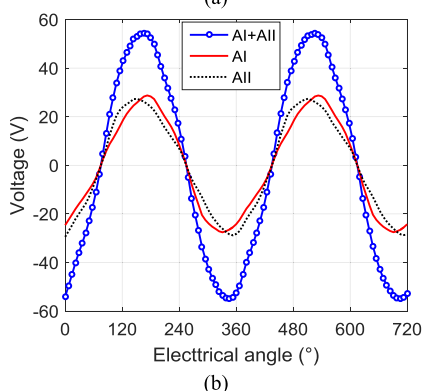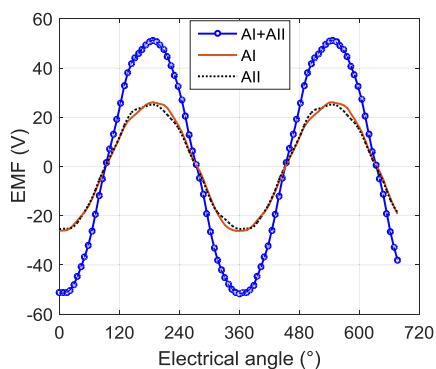
FIGURE 5. Modular structure.

(a)

(b)

FIGURE 6. No-load EMF and load voltage. (a) No-load EMF. (b) On-load voltage.
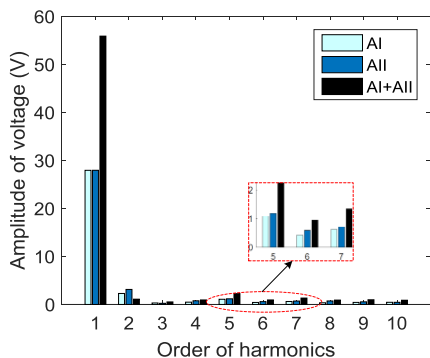
FIGURE 7. Harmonics of the voltages.

FIGURE 8. Thrust curves of the modular and non-modular CP-PMLSM.
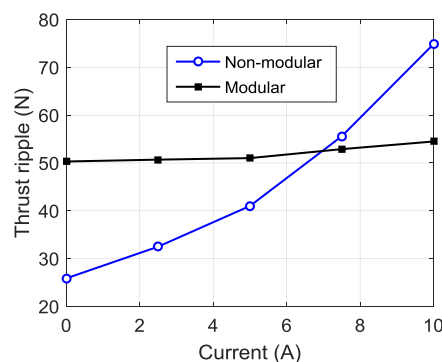
FIGURE 9. Peak-to-peak values of thrust ripple vary as current.

Fig. 9 shows the variation of the peak-to-peak thrust ripple with the load current. The influence of the armature current on the thrust ripple is reduced significantly with respect to that of the non-modular structure. The harmonics of the thrust ripple when the load-current of the modular CP-PMLSM is 5 A were analyzed. For the aforesaid load current, the third-order thrust ripple that originates from the second voltage harmonic voltage is reduced by over 8 times, from 11.69 N to 1.34 N.

In Fig. 7, the 4th, 6th, 8th harmonics for AI + AII seems additive, which seems incompatible with (12). We consider the reason is the influence of the end effect. For the sectional motors I and II, the end effect also causes even magnetic field components, whose electrical angles may not differ strictly 180°. Besides, the increased core ends may due to the increasing of detent force, which is analyzed as follows.

bigger than that of the non-modular motor. At the same time, the frequency of the thrust fluctuation is transformed from 120° to about 180°, which is equivalent to that of a PMLSM with a NS pole.
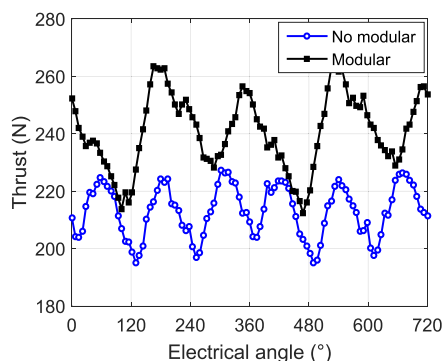
If the magnetic regulating structure adopts non-magnetic material, the number of the core-ends in the primary will double from 2 to 4. From equation (4), the whole detent force can then be expressed as:

$$
\begin{aligned}
f_{detent} &= f_{detentI} + f_{detentII} \\
&= \sum_{n=1}^{\infty} F_{nI} \sin \frac{2n\pi}{\tau}(z + \frac{\tau}{2}) \\
&\quad + \sum_{n=1}^{\infty} F_{nII} \sin \frac{2n\pi}{\tau}(z + \frac{\tau}{2} + 11\tau)
\end{aligned} \tag{10}
$$

where $f_{detentI}$ and $f_{detentII}$ denote the detent force of the sectional motor I and motor II, F_{nI} and F_{nII} denote the amplitude of n-th components of $f_{detentI}$ and $f_{detentII}$.

It can be deduced that the phase angles of the same order harmonics of $f_{detentI}$ and $f_{detentII}$ are identical, and the detent force of the modular structure increases with respect to that of the non-modular structure. Specifically, the amplitude of the second harmonic which originates from the end effects increases from 2.39 N to 15.5 N.
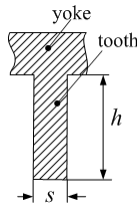

FIGURE 10. Magnetic regulating tooth structure.

IV. OPTIMIZATION OF THE MAGNETIC REGULATING STRUCTURE AND END-TEETH TO REDUCE DETENT FORCE–STEP II

A. MAGNETIC REGULATING TOOTH STRUCTURE

After suppressing the thrust ripple coming from the armature current in the first step, the magnetic regulating structure is optimized in order to reduce the detent force in the second step. On the basis of the foregoing analysis in Section III, the core- end number for the modular motor can be reduced by adopting a magnetically conductive core for the magnetic regulating structure. In addition, for the modular design, the length of the primary core and the structure of the end-teeth act together on the magnetic flux distribution and affect the detent force. Thus the magnetic regulating structure and the end-teeth should be considered and optimized synthetically. The magnetic regulation structure is first designed as a yoke and tooth structure, as shown in Fig. 10. If the height of the tooth (h) is set to zero, it corresponds to the regulating structure simply consisting of a yoke (i.e. no tooth). Contrary to the previously proposed modular structure that adopts non-magnetic material [23]–[27], the modular regulating structure proposed in this paper is magnetically permeable and also integrated with the primary cores of sectional motors I and II.

Through calculation, it is observed that the size of the end-teeth has little influence on the average thrust, but has a more significant effect on the thrust fluctuation, which is similar to what is observed in a conventional PMLSM with a NS pole. For the primary-mover PMLSM, the width and height of the end-teeth, together with the width of the end-slot can be optimized in order to reduce the detent force. Considering not extending the length of the primary and decreasing the effective motion range, the height of the end- teeth h_{te} is selected as one of the key optimization parameters. Likewise, the constituent geometries of the regulating tooth structure, namely the width s and height h, as shown in Fig. 10, are also important optimization parameters. The initial ranges of these three geometric parameters are listed in Table 2, and discussed in detail in the following section.

TABLE 2. Three geometric parameters.

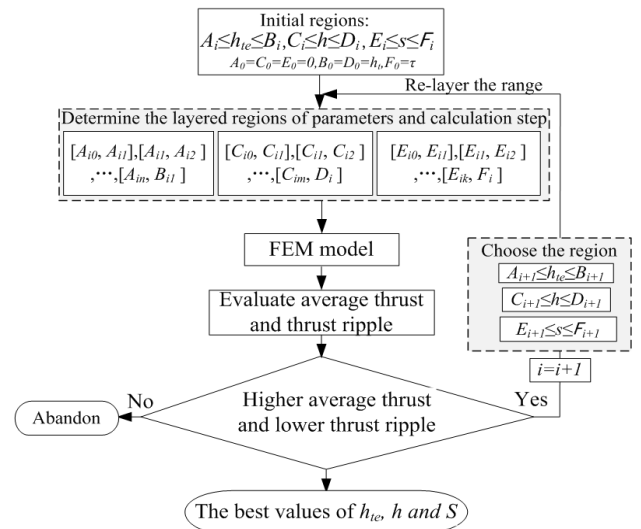| Symbol	ITEMS	Initial Range
h_{te}	Height of ended teeth (mm)	$0 \leq h_{te} \leq h_t$
h	Height of the magnetic regulating teeth (mm)	$0 \leq h \leq h_t$
s	Width of the magnetic regulating teeth (mm)	$0 \leq S \leq \tau$

FIGURE 11. Layered optimization process.

B. LAYERED OPTIMIZATION OF THE MAGNETIC REGULATING TOOTH AND ENDED TEETH

A layered optimization is processed as shown in Fig. 11. The initial values of the parameters h_{te}, h and s are divided into several regions, with the number for each denoted by n, m and, k, respectively. Meanwhile, the calculation steps are set for each region. FEM models are applied, and the thrust characteristic results, including the average thrust and thrust ripple, are obtained and compared. Following this the suitable regions are selected, whereas the unsatisfactory regions are abandoned. For example, Fig. 12 shows the thrust curves following the change of the magnetic regulating tooth height (h) when the end- teeth height h_{te} adopts different values (the
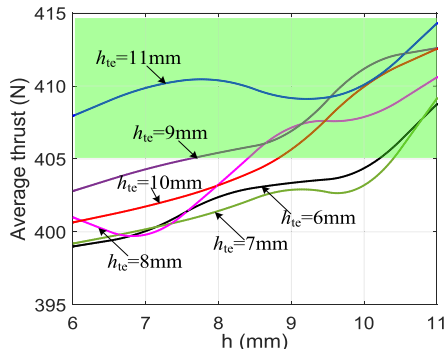
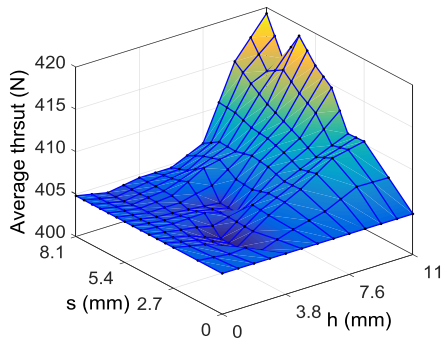**FIGURE 12.** Family of average thrust curves vary as *h*.

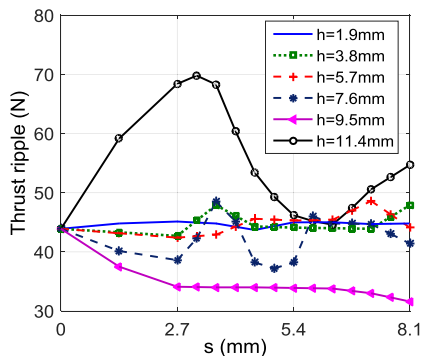**FIGURE 13.** Average thrust changes as the height and width of the tooth.

FIGURE 14. Thrust ripples changing as tooth width with different height.

FIGURE 15. Thrust and its ripple vary as the ratio of the W_p to W_C.

Fig. 13, it can be observed that the bigger the values of *h* or *s*, the higher is the average thrust. Moreover the average thrust can get a significantly relative larger value when *h* and *s* are above 8 mm and 3.6 mm respectively. Fig. 14 shows the variation of the peak-to-peak value of the thrust ripple with the tooth width for different tooth heights. The thrust ripple varies significantly for different tooth heights. For example when the height *h* is 11.4 mm, the thrust fluctuation is highest and it fluctuates with the tooth width *s*. On the other hand, when the tooth height *h* is 9.5 mm, the thrust ripple is much less sensitive to the tooth width variation, being less than 34 N when the width *s* is within the range of 2.7 mm to 8.1 mm, and reaching a minimum value of 31.6 N for a tooth width of 8.1 mm.

C. POLE OPTIMIZATION

In the previous analysis, both the widths of the PM and core poles are 6.5 mm. However, the relative sizes of the PM and core poles are more sensitive with respect to the traditional North-South PM poles. In light of this, optimization is also carried out for different PM widths W_p and core widths W_c. The values of W_c ranging from 5.7 mm to 8.1 mm, as well as the corresponding changes of the values of corresponding change, are analyzed. The results indicate that when the value of W_c is with a range of 6.1 mm to 6.5 mm, the motor can obtain a relative large average thrust and low thrust ripple.

However the thrust ripple variation with the magnet width W_p is markedly different for the considered cases of core widths W_c. Fig. 15 shows the variation of the average thrust and the peak-to-peak thrust ripple with the magnet-width W_p,

width of the magnetic regulating tooth keeps constant). If the output requirements are set as that the average thrust when the current density is 10 A/mm² should be larger than 405 N, only the regions highlighted in green in the Figures were selected for the next layer optimization. For the modular CP-PMLSM in this paper, the end teeth achieves the best effects in improving the average thrust when their height h_{te} ranges from 8 mm to 11 mm.

For the subsequent layer calculation, the selected regions are divided afresh and provided for the FEM model. The aforementioned cycle is repeated again and again until the best values of the parameters are determined. Figs. 13 and 14 show how the height and width of the magnetic regulating tooth effect the average thrust and thrust ripple when the end tooth height is at its optimal value of 8 mm. From
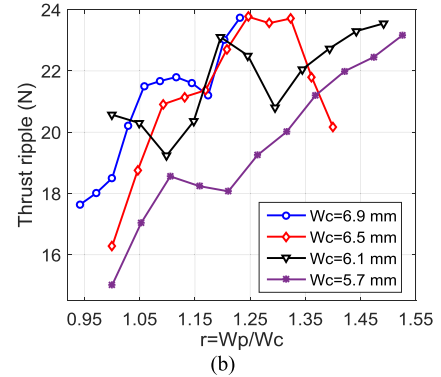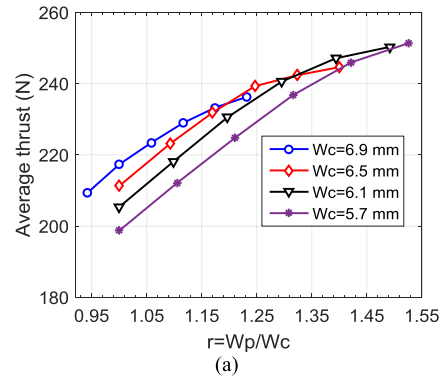
FIGURE 16. Thrust ripple changes as current. (a) Average thrust. (b) Thrust ripple.
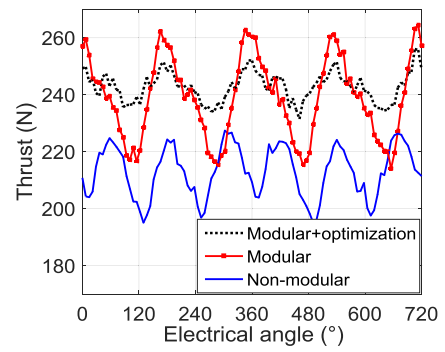

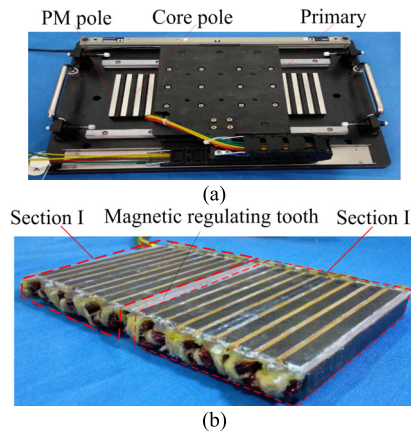
FIGURE 17. Thrust curves when the motors in the rated load condition.

FIGURE 18. Prototype of modular CP-PMLSM. (a) Whole motor. (b) Primary.
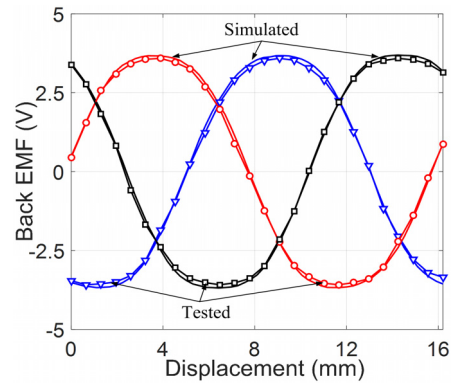

FIGURE 19. EMF waveform of the prototype.

when the core-width W_c is selected as 6.5 mm. As the magnet width W_p is increased from 8 mm to 10 mm, the average thrust increases firstly, reaches a peak of around 470 N when W_p is around 8.6 mm, and then decreases. Apparently, the average thrust has been increased by optimizing the geometrical parameters of poles. As the magnet width is increased the thrust ripple decreases firstly, reaches a minimum of 12.8 N when W_p is also 8.6 mm, and then increases for wider magnet dimensions. Taking into account the important system consideration of reducing PM consumption, enhancing average thrust and reducing thrust ripple, the optimal width of the PM W_p and the optimal width of the core pole W_c are determined as 8.6 mm and 6.5 mm respectively.

Fig. 16 presents the variation of the average thrust and the thrust ripple with the load current for the non-modular motor and for the modular motors (before and after the described optimization procedure). Through the proposed modular design and two-step refinement procedure the average thrust increases slightly and the thrust ripple reduces markedly. Moreover, a minimal-thrust ripple design, in which the thrust ripple does not increase with load current is achieved for the CP-PMLSM. Fig. 17 shows thrust curves in which the differences of the fluctuating frequencies, peak-to-peak values of the thrusts, and the average thrusts among the three motors can be observed.

V. TEST OF A MODULAR CP-PMLSM

A modular CP-PMLSM was developed and prototyped, the secondary of which has a consequent-pole structure, while the primary is concentrated-wound and modular, as shown in Fig. 18. Most parameters of prototype are as listed in Table 2. The difference is that the height of PM is modified to 3.5 mm to improve anti-demagnetization ability. After the comprehensive optimization as described above, the width and height of the magnetic regulating tooth are designed as 8.1 mm and 9.5 mm, respectively. A servo motor system integrated with a ball screw mechanism was connected to the mover of the PMLSM by a pull pressure sensor.

By having the servomotor system move the prototype linearly, the no-load back EMF waveforms could be obtained as shown in Fig. 19. The amplitudes of the EMF are basically
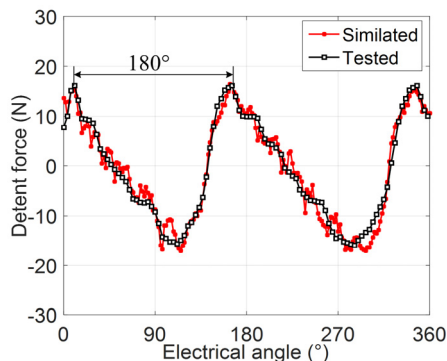
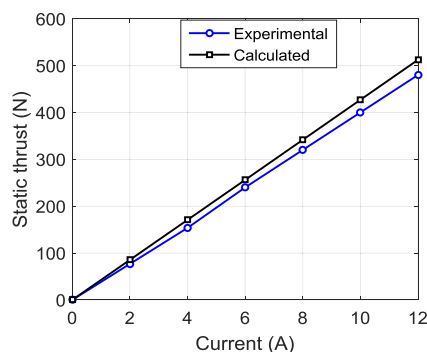**FIGURE 20.** Detent force varying as electrical angle.

FIGURE 21. Static thrust variation with current.

equal with a 120° phase shift. The presence of high-order harmonics can also be observed from the waveforms. The tested and calculated waveforms agree with each other basically. The amplitudes of the tested back EMF are a little lower than those of the calculated results. The detent force characteristic can be read through the pressure sensor, as shown Fig. 20. It fluctuates with a single cycle as the mover travels 180°, which is consistent with the theory and analysis presented in Sections II and III. From the same figure, the measured detent force matches closely to the calculated one. There is a little difference, which be due to multi factors, including machining errors, impact of friction, inconsistency of the material performance, or precision of the sensor.

When the windings are powered with a DC current, the mover can output static thrust, which varies with the mover position as it is dragged. When the thrust is biggest, the current is close to the quadrature-axis current. Thus the static thrust which varies as the current can be obtained, as shown in Fig. 21. The test results broadly correspond with those calculated, with the discrepancy increasing for higher currents up to 8% at the current of 12 A. This possibly indicates magnetic saturation and the need for improved magnetic material characterization at high induction levels, but could well be due to other factors, including transverse edge effects, assembly tolerance, PM thermal effects.

VI. CONCLUSION
The thrust ripple of CP-PMLSMs was investigated in detail in this paper. A FEM model was adopted to analyze the

components of the thrust ripple, which mainly contain the ripple from the second voltage harmonic and the detent force rooted in end-slot effects. To suppress the thrust ripple, a two-step design was proposed and processed.

In the first step, by setting the modular regulating structure and rewinding the same-phase coils in the resulting two sectional motors, the ripple increase with the winding current is eliminated, and for the case-study motor maintains a constant value. In the second step, a magnetic permeable material is adopted to reduce the end-number. Within this step the geometrical parameters of the magnetic regulating tooth and end-teeth are synthetically optimized to minimize the detent force. Moreover, the optimal values of core pole span and magnet span are determined to reduce the cogging force and improve the average thrust. With the procedure proposed in this research, the thrust ripple achieves a smaller value with respect to the modular CP-PMLSM for all load conditions.

REFERENCES
[1] S.-U. Chung *et al.*, "Design and experimental validation of doubly salient permanent magnet linear synchronous motor for precision position control," *Mechatronics*, vol. 23, pp. 172–181, Mar. 2013.

[2] H. Wang *et al.*, "A novel consequent-pole hybrid excited vernier machine," *IEEE Trans. Magn.*, vol. 53, no. 11, Dec. 2017, Art. no. 8112304.

[3] C. Shi, D. Li, R. Qu, H. Zhang, Y. Gao, and Y. Huo, "A novel linear permanent magnet vernier machine with consequent-pole permanent magnets and Halbach permanent magnet arrays," *IEEE Trans. Magn.*, vol. 53, no. 11, pp. 1–4, Nov. 2017.

[4] S.-U. Chung, J.-W. Kim, B.-C. Woo, D.-K. Hong, J.-Y. Lee, and D.-H. Koo, "A novel design of modular three-phase permanent magnet vernier machine with consequent pole rotor," *IEEE Trans. Magn.*, vol. 47, no. 10, pp. 4215–4218, Oct. 2011.

[5] H. Hua, Z. Q. Zhu, and H. Zhan, "Novel consequent-pole hybrid excited machine with separated excitation stator," *IEEE Trans. Ind. Electron.*, vol. 63, no. 8, pp. 4718–4728, Apr. 2016.

[6] Y. Gao, R. Qu, D. Li, J. Li, and G. Zhou, "Consequent-pole flux-reversal permanent-magnet machine for electric vehicle propulsion," *IEEE Trans. Appl. Supercond.*, vol. 26, no. 4, Oct. 2016, Art. no. 5200105.

[7] M. Takemoto, "Basic characteristic of a two-unit outer rotor type bearingless motor with consequent pole permanent magnet structure," in *Proc. Int. Power Electron. Conf. (IPEC)*, Hiroshima, Japan, 2014, pp. 1000–1005.

[8] E. Severson, R. Nilssen, T. Undeland, and N. Mohan, "Dual-purpose no-voltage winding design for the bearingless AC homopolar and consequent pole motors," *IEEE Trans. Ind. Appl.*, vol. 51, no. 4, pp. 2884–2895, Jul./Aug. 2015.

[9] S.-U. Chung, S.-H. Moon, D.-J. Kim, and J.-M. Kim, "Development of a 20-pole–24-slot SPMSM with consequent pole rotor for in-wheel direct drive," *IEEE Trans. Ind. Electron.*, vol. 63, no. 1, pp. 302–309, Jan. 2016.

[10] R. T. Ugale and B. N. Chaudhari, "Rotor configurations for improved starting and synchronous performance of line start permanent-magnet synchronous motor," *IEEE Trans. Ind. Electron.*, vol. 64, no. 1, pp. 138–148, Jan. 2017.

[11] M.-T. Chui, J.-A. Chiang, Z.-L. Gaing, and C.-M. Lin, "Design of a novel consequent-pole interior PM motor for applying to refrigerant compressor," in *Proc. Int. Conf. Elect. Mach. Syst. (ICEMS)*, Tokyo, Japan, 2016, pp. 1–5.

[12] S.-U. Chung, J.-W. Kim, B.-C. Woo, D.-K. Hong, J.-Y. Lee, and D.-H. Koo, "Force ripple and magnetic unbalance reduction design for doubly salient permanent magnet linear synchronous motor," *IEEE Trans. Magn.*, vol. 47, no. 10, pp. 4207–4210, Oct. 2011.

[13] F. Tootoonchian and Z. Nasiri-Gheidari, "Cogging force mitigation techniques in a modular linear permanent magnet motor," *IET Elect. Power Appl.*, vol. 10, no. 7, pp. 667–674, 2016.

[14] X. Huang, Q. Tan, Q. Wang, and J. Li, "Optimization for the pole structure of slot-less tubular permanent magnet synchronous linear motor and segmented detent force compensation," *IEEE Trans. Appl. Supercond.*, vol. 26, no. 7, pp. 1–5, Oct. 2016.

[15] J. W. K. L. Zhao and P. B. J. Chen Huang, "Reduction of detent force in permanent magnet linear synchronous motor with double secondary side," in *Proc. Int. Conf. Elect. Mach. Syst. (ICEMS)*, Hangzhou, China, 2014, pp. 1274–1277.

[16] Y.-S. Kwon and W.-J. Kim, "Detent-force minimization of double-sided interior permanent-magnet flat linear brushless motor," *IEEE Trans. Magn.*, vol. 52, no. 4, Apr. 2016. Art. no. 8201609.

[17] Y. Bai, T. Yang, and B. Kou, "Reducing detent force and three-phase magnetic paths unbalance of PM linear synchronous motor using modular primary iron-core structure," in *Proc. Int. Conf. Elect. Mach. Syst. (ICEMS)*, Hangzhou, China, 2014, pp. 1743–1748.

[18] F. Cupertino, P. Giangrande, G. Pellegrino, and L. Salvatore, "End effects in linear tubular motors and compensated position sensorless control based on pulsating voltage injection," *IEEE Trans. Ind. Electron.*, vol. 58, no. 2, pp. 494–501, Feb. 2011.

[19] C. Yang, T. Ma, Z. Che, and L. Zhou, "An adaptive-gain sliding mode observer for sensorless control of permanent magnet linear synchronous motors," *IEEE Access*, vol. 6, pp. 3468–3478, Dec. 2017.

[20] S.-U. Chung and J.-M. Kim, "Double-sided iron-core PMLSM mover teeth arrangement design for reduction of detent force and speed ripple," *IEEE Trans. Ind. Electron.*, vol. 63, no. 5, pp. 3000–3008, May 2016.

[21] Y. W. Zhu, S. G. Lee, K. S. Chung, and Y. H. Cho, "Investigation of auxiliary poles design criteria on reduction of end effect of detent force for PMLSM," *IEEE Trans. Magn.*, vol. 45, no. 6, pp. 2863–2866, Jun. 2009.

[22] N. Baatar, H. S. Yoon, M. T. Pham, P. S. Shin, and C. S. Koh, "Shape optimal design of a 9-pole 10-slot PMLSM for detent force reduction using adaptive response surface method," *IEEE Trans. Magn.*, vol. 45, no. 10, pp. 4562–4565, Oct. 2009.

[23] B. Li, J. Zhao, X. Liu, Y. Guo, H. Hu, and J. Li, "Detent force reduction of an arc-linear permanent-magnet synchronous motor by using compensation windings," *IEEE Trans. Ind. Electron.*, vol. 64, no. 4, pp. 3001–3011, Apr. 2017.

[24] R. Cao, M. Cheng, C. Mi, W. Hua, and W. Zhao, "Comparison of complementary and modular linear flux-switching motors with different mover and stator pole pitch," *IEEE Trans. Magn.*, vol. 49, no. 4, pp. 1493–1504, Apr. 2013.

[25] R. Cao, M. Cheng, C. C. Mi, and W. Hua, "Influence of leading design parameters on the force performance of a complementary and modular linear flux-switching permanent-magnet motor," *IEEE Trans. Ind. Electron.*, vol. 61, no. 5, pp. 2165–2175, May 2014.

[26] R. Cao, M. Cheng, and W. Hua, "Investigation and general design principle of a new series of complementary and modular linear FSPM motors," *IEEE Trans. Ind. Electron.*, vol. 60, no. 12, pp. 5436–5446, Dec. 2013.

[27] R. Cao *et al.*, "Modeling of a complementary and modular linear flux-switching permanent magnet motor for urban rail transit applications," *IEEE Trans. Energy Convers.*, vol. 27, no. 2, pp. 489–497, Jun. 2012.

XUZHEN HUANG (M'14) received the B.E., M.E. and Ph.D. degrees from the Harbin Institute of Technology, Harbin, China, in 2006, 2008, and 2012, respectively.

She is with the Jiangsu Key Laboratory of New Energy Generation and Power Conversion, Nanjing University of Aeronautics and Astronautics, where she is currently an Associate Professor. Her current research interest includes the linear permanent magnet synchronous motors and the thermal analysis of motors.

JING LIANG received the B.E. degree in electrical engineering from the Hubei University of Technology, Hubei, China, in 2017.

He is currently pursuing the M.E. degree with the Nanjing University of Aeronautics and Astronautics. His current research interest is permanent magnet synchronous linear motors.

BO ZHOU received the B.S. degree from Zhejiang University, Hangzhou, China, in 1983, the M.S. degree from Chongqing University, Chongqing, China, in 1986, and the Ph.D. degree from the Nanjing University of Aeronautics and Astronautics (NUAA), Nanjing, China, in 2000. He was with NUAA. He is currently a Professor with the College of Automation Engineering, NUAA, and the Director of the Jiangsu Key Laboratory of New Energy Generation and Power Conversion. His research interests include power converter, electrical machine driving systems, and renewable power systems.

CHENGMING ZHANG received the B.E., M.E., and D.E. degrees from the Harbin Institute of Technology (HIT), China, in 2005, 2007, and 2013, respectively.

Since 2013, he has been a Lecturer with the School of Electrical Engineering and Automation, HIT. His research areas include high-efficiency motor systems, and energy conversion and control.

LIYI LI (M'09) received the B.E., M.E., and D. E. degrees from the Harbin Institute of Technology (HIT), Harbin, China, in 1991, 1995, and 2001, respectively.

Since 2004, he has been a Professor with the School of Electrical Engineering and Automation, HIT. He has authored or co-authored over 110 technical papers. He holds 50 patents. His research areas are in the control and drive of high-speed permanent magnet synchronous motors and linear motors.

DAVID GERADA received the Ph.D. degree in high-speed electrical machines from the University of Nottingham, Nottingham, U.K., in 2012. He was with the Research and Development Department, Cummins, first as an Electromagnetic Design Engineer from 2007 to 2012, and then as a Senior Electromagnetic Design Engineer and the Innovation Leader from 2012 to 2016. At Cummins, he pioneered the design and development of high-speed electrical machines, transforming a challenging technology into a reliable one suitable for the transportation market while establishing industry-wide used metrics for such machinery. In 2016, he joined the University of Nottingham as a Senior Fellow in electrical machines, responsible for developing the state-of-the-art electrical machines for future transportation which push existing technology boundaries while propelling the new technologies to higher technology readiness levels. He is a Chartered Engineer in U.K. He is a member of the Institution of Engineering and Technology.

• • •